A PV-Battery Three-Port Wireless Charger for Unmanned Aerial Vehicles

Siyi Yao, Xinling Wang, *Student Member, IEEE*, Junrui Liang, *Senior Member, IEEE*, Haoyu Wang, *Senior Member, IEEE*, and Minfan Fu, *Senior Member, IEEE*

***Abstract*—This letter introduces a photovoltaic (PV)-battery wireless charger tailored for unmanned aerial vehicles (UAVs), enabling seamless automatic charging. Sharing the resonant tank enhances efficiency while reducing the number of resonant components required. Employing a bridge converter allows for versatile modulations, facilitating various functions including output regulation, maximum power point tracking, and zero voltage switching. Experimental validation involves the construction of a 200-W prototype, demonstrating a peak efficiency of 92.6% for the three-port converter and supporting four distinct charging modes.**

***Index Terms*—Integrated power converter, photovoltaic (PV), unmanned aerial vehicle (UAV), wireless charger.**

I. Introduction

THE rising popularity of unmanned aerial vehicles (UAVs) is attributed to their agility, small size, and light weight, which make them ideal for tasks such as inspections, agriculture, and damage assessment [1], [2], [3]. However, despite their advantages, UAVs are limited by their reliance on power, often draining their batteries quickly due to the demands of flight. Traditional methods of battery swapping require human intervention, posing challenges for autonomous operations in remote or inaccessible areas. As a solution, inductive power transfer (IPT) emerges as an appealing option to extend the autonomous operational lifespan [4], [5].

In contrast to wireless charging for consumer electronics, UAVs often operate in remote locations such as mountains and farmlands. Therefore, relying on renewable energy sources instead of the power grid becomes a more logical choice. For instance, photovoltaic (PV) technology is utilized to power the IPT by incorporating a dc/dc converter [6]. To address the variability of sunlight, a battery is directly integrated into the dc bus to ensure a consistent output [7], [8]. By connecting the battery to the dc bus through another converter, three power ports are controlled independently [9]. Moreover, the synergy between PV and battery allows for more efficient charging and diverse charging modes [10]. However, the advantages of these systems rely on employing multiple power stages, which would increase costs and losses.

This article presents an innovative PV-battery wireless charging system designed specifically for UAVs. The proposed topology utilizes a conventional bridge converter at each power port, with power coupling achieved through a central ac resonant tank, forming a high-order three-port resonant converter. With tank integration, power transfer between ports circumvents multiple stages, leading to a reduction in passive components and an improvement in efficiency. Circuit-model-based analysis is employed to investigate transfer characteristics, converter design, and modulation techniques. Additionally, the integrated power converter holds promise for various scenarios requiring energy harvesting and wireless charging.

II. Three-Port Wireless Charger

The proposed charger is illustrated in Fig. 1(a). The PV functions as a power source, providing P_{pv}, while the UAV acts as the load, consuming P_{uav}. The power flow of both are unidirectional. The battery is required to supply bidirectional power, P_{bat}. Utilizing a bridge inverter, the PV panel can generate regulated voltage v_1 to excite one ac terminal, while the battery provides similar excitation with v_2. The ac voltage at the UAV terminal is represented as v_3. Terminal currents at the various ac ports are denoted as i_1, i_2, and i_3 respectively. Power from the PV, battery, and UAV is interconnected through the three-port resonant tank. It comprises four ac components, i.e., a transformer with turn ratio n and magnetizing inductance L_m, an inductive coupler with self-inductance L_p and L_s, mutual inductance M, and two compensation capacitors C_p and C_s.

The equivalent circuit can be simplified as depicted in Fig. 2, where all state variables are represented in their phasor form. For instance, $\mathbf{V_1}$ denotes the phasor form of v_1, with V_1 indicating its magnitude. The equivalent ac resistance for the UAV side

Received 14 June 2024; revised 12 September 2024; accepted 24 October 2024. Date of publication 19 November 2024; date of current version 30 April 2025. This work was supported in part by the National Natural Science Foundation of China under Grant 52477013 and in part by Lingang Laboratory under Grant LG-GG-202402-06-10. *(Siyi Yao and Xinlin Wang are co-first authors.) (Corresponding author: Minfan Fu.)*

Siyi Yao is with the School of Information Science and Technology, ShanghaiTech University, Shanghai 201210, China and also with Lin Gang Laboratory, Shanghai 200031, China.

Xinling Wang is with the School of Information Science and Technology, ShanghaiTech University, Shanghai 201210, China.

Junrui Liang, Haoyu Wang, and Minfan Fu are with the School of Information Science and Technology, ShanghaiTech University, Shanghai 201210, China, and also with Shanghai Engineering Research Center of Energy Efficient and Custom AI IC, Shanghai 201210, China (e-mail: fumf@shanghaitech.edu.cn).

Digital Object Identifier 10.1109/TIE.2024.3493197

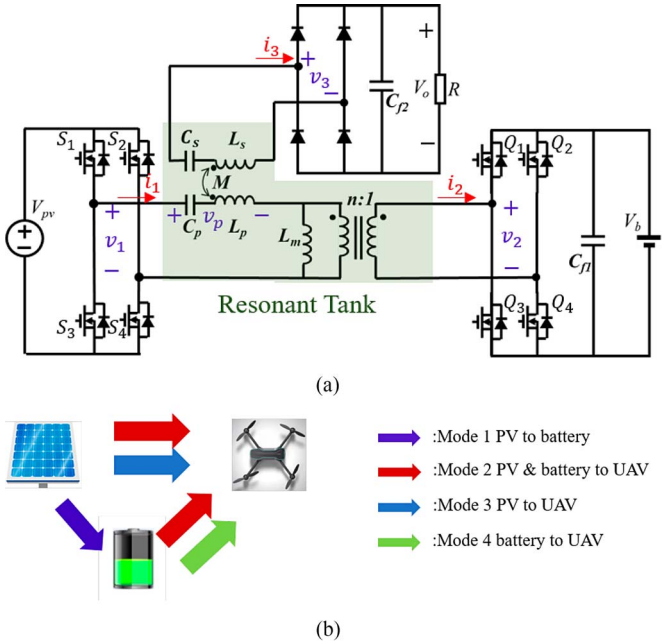

Fig. 1. Three-port wireless charger. (a) Topology. (b) Four modes.

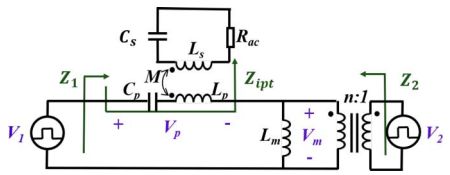

Fig. 2. Equivalent circuit.

is $R_{\text{ac}} = 8R/\pi^2$. There are four modes as shown in Fig. 1(b). In the absence of the UAV, mode 1 is delineated for direct charging of the battery by the PV. The system transforms into an LLC converter, which could use L_m for load-independent zero voltage switching (ZVS) operation. Upon activation of all ports, the PV and battery jointly charge the UAV, termed mode 2. The PV alone suffices to power the UAV, termed mode 3. In the absence of sunlight, the battery operates as the single source under mode 4. Modes 3 and 4 are considered special cases of mode 2 by shorting either $\mathbf{V_1}$ or $\mathbf{V_2}$.

In Fig. 3, θ_1 is the phase between two legs, which leads to a typical three-level voltage source v_1. Similarly, the inverter of the battery would offer a controlled voltage source v_2 by changing θ_2. Their voltage magnitude are as follows:

$$V_1 = \int_0^{T_s} \sin\omega t \cdot v_1(t)dt = \frac{4}{\pi} V_{\text{pv}} \cos\frac{\theta_1}{2}$$
$$V_2 = \int_0^{T_s} \sin\omega t \cdot v_2(t)dt = \frac{4}{\pi} V_b \cos\frac{\theta_2}{2}. \quad (1)$$

The phase difference between $\mathbf{V_1}$ and $\mathbf{V_2}$ is denoted as α $(=\pi)$, and this phase is not utilized for modulation. When $\mathbf{V_1}$ is considered as the reference (i.e., $\mathbf{V_1} = V_1\angle 0$), $\mathbf{V_2}$ is represented as $\mathbf{V_2} = V_2\angle\pi = -V_2\angle 0$. The voltage across L_m

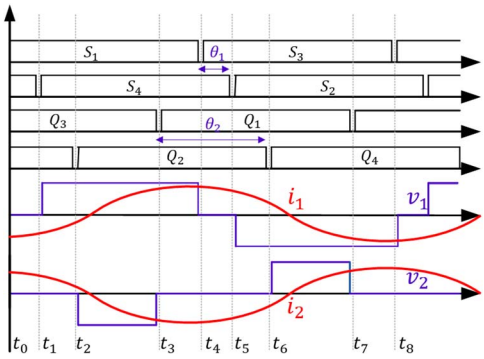

Fig. 3. Gate signals and typical waveforms.

is clamped as $\mathbf{V_m} = n\mathbf{V_2}$. The voltage for the PV-side resonant tank is denoted as $\mathbf{V_p}$ and is expressed as

$$\mathbf{V_p} = \mathbf{V_1} - \mathbf{V_m} = \frac{4}{\pi}\left(V_{\text{pv}} \cos\frac{\theta_1}{2} + nV_b \cos\frac{\theta_2}{2}\right)\angle 0. \quad (2)$$

It's evident that $\mathbf{V_p}$ is always in phase with $\mathbf{V_1}$.

A nominal resonance frequency, denoted as f_r, is defined based on the characteristics of the two series resonant tanks

$$f_r = 1/(2\pi\sqrt{L_pC_p}) = 1/(2\pi\sqrt{L_sC_s}). \quad (3)$$

The switching frequency of two inverters is f $(=\omega/2\pi)$. It's worth noting that f may not necessarily be equal to f_r. Based on circuit theory, the state equations are given as

$$\begin{bmatrix}\mathbf{V_p}\\ \mathbf{V_3}\end{bmatrix} = \begin{bmatrix}1 & -n\\ \frac{\omega M R_{\text{ac}}}{(Z_pZ_s+\omega^2M^2)} & \frac{-n\omega M R_{\text{ac}}}{(Z_pZ_s+\omega^2M^2)}\end{bmatrix}\begin{bmatrix}\mathbf{V_1}\\ \mathbf{V_2}\end{bmatrix} \quad (4)$$

$$\begin{bmatrix}\mathbf{I_p}\\ \mathbf{I_3}\end{bmatrix} = \begin{bmatrix}\frac{1}{\omega^2M^2/Z_s+Z_p} & \frac{-n}{\omega^2M^2/Z_s+Z_p}\\ \frac{\omega M}{Z_pZ_s+\omega^2M^2} & \frac{-n\omega M}{Z_pZ_s+\omega^2M^2}\end{bmatrix}\begin{bmatrix}\mathbf{V_1}\\ \mathbf{V_2}\end{bmatrix} \quad (5)$$

where $\mathbf{Z_p}$ and $\mathbf{Z_s}$ are defined as the net impedance of tanks L_pC_p and L_sC_s respectively

$$\begin{cases}\mathbf{Z_p} = j\omega L_p + 1/(j\omega C_p)\\ \mathbf{Z_s} = j\omega L_s + 1/(j\omega C_s) + R_{\text{ac}}.\end{cases} \quad (6)$$

Using the above equations, all the state variables can be derived. For example, the output voltage is solved as

$$V_o = \frac{\omega M}{Z_pZ_s+\omega^2M^2} \cdot \left(V_{\text{pv}} \cos\frac{\theta_1}{2} + nV_b \cos\frac{\theta_2}{2}\right) \cdot \frac{8R}{\pi^2}. \quad (7)$$

When all the voltage or current are solved, the terminal power could be derived as follows:

$$P_{\text{uav}} = {V_o}^2/R \quad (8)$$

$$P_{\text{pv}} = \frac{V_{\text{pv}} \cos\left(\frac{\theta_1}{2}\right)\left[V_{\text{pv}} \cos\left(\frac{\theta_1}{2}\right) + nV_b \cos\left(\frac{\theta_2}{2}\right)\right] R}{2\omega^2M^2}. \quad (9)$$

III. Modulation and Design Consideration

The proposed converter integrates frequency and phase modulation to fulfill various practical objectives, such as adjusting the output voltage at the UAV terminal, facilitating maximum power point tracking (MPPT) at the PV terminal, and achieving soft-switching for all transistors. The controllable P_{uav} indicates

TABLE I
PARAMETERS OF AN EXAMPLE SYSTEM

Symbol	Value	Symbol	Value	Symbol	Value
V_{pv}	36 V	L_p, L_s	33 μH	f_r	85 kHz
V_b	24 V	C_p, C_s	107 nF	n	1.5
M	[18 μH, 22 μH]	L_m	170 μH	f	150 kHz

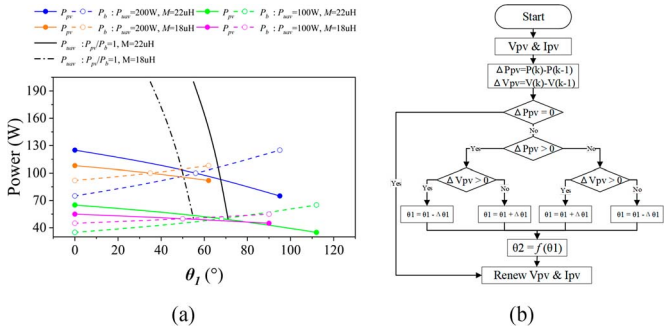

(a) (b)

Fig. 4. (a) Output regulation and MPPT by tuning θ_1. (b) MPPT algorithm.

the output modulation capability, and P_{pv} should be controlled for MPPT. Therefore, (8) and (9) actually defines two equality constrains for the control variables. The last objective is to ensure soft-switching for active bridges. The dual active bridge converters have been widely used and well studied. The ZVS condition could be represented by the phase of bridge output voltage. In Fig. 2, θ_{Z1} and θ_{Z2} are the phase of $\mathbf{Z_1}$ and $\mathbf{Z_2}$ respectively, the ZVS operation need to meet

$$\theta_{Z1} > \theta_1/2, \theta_{Z2} > \theta_2/2. \tag{10}$$

An example waveform is shown in Fig. 3, when $\theta_1 = 30°$, $\theta_2 = 70°$, $\theta_{Z1} = \theta_{Z2} = 40°$. For the PV-side bridge, S_1, S_2, S_3, and S_4 are able to achieve ZVS turn ON at t_0, t_5, t_4, and t_1 respectively. So as for the battery-side bridge.

For better illustration, an example system is given in Table I to discuss the modulation. When f is fixed at 150 kHz, the dual phases (θ_1 & θ_2) would modulate P_{pv} and P_{bat} and finally offer a wide P_{uav} (=$P_{\text{pv}} + P_{\text{bat}}$). For a specific P_{uav}, there is still one control freedom left to modify the power ratio between P_{pv} and P_{bat}. As shown in Fig. 4(a), when the output power is 200 W, the blue soild line means P_{pv} and the dot one represents P_{bat}. It shows that θ_1 is used to change the power distribution between PV and battery, which equally means MPPT could be achieved by controlling P_{pv} at its target level. Note that θ_2 depends on θ_1 due to the fixed P_{uav}. When P_{uav} changes to 100 W, the conclusion is similar. When M diminishes to 18 μH, there is a reduction in the output capacity, yet the control effectiveness for MPPT remains evident, as illustrated by the orange and green curves. When sweeping P_{uav}, the phase variation is depicted by the black lines. The MPPT requires one control freedom to regulate P_{pv}, which is denoted as θ_1. The widely recognized tracking algorithm is utilized, as illustrated in Fig. 4(b).

The choice of the switching frequency f must account for the ZVS requirement. Based on (7) and (9), θ_1 and θ_2 are determined as follows:

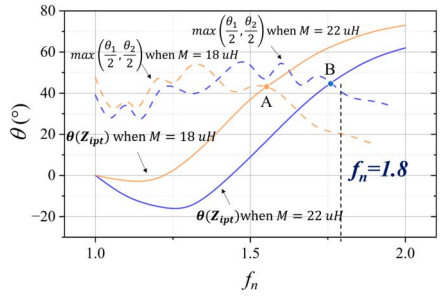

Fig. 5. Design of f based on ZVS boundary.

$$\theta_1 = 2\cos^{-1}\left[\frac{16P_{\text{pv}}\omega^3M^3}{V_{\text{pv}}V_o\pi^2(Z_pZ_s+\omega^2M^2)}\right] \tag{11}$$

$$\theta_2 = 2\cos^{-1}\left[\frac{\frac{V_o\pi^2(Z_pZ_s+\omega^2M^2)}{8\omega MR} - V_{\text{pv}}\cos(\theta_1/2)}{nV_b}\right]. \tag{12}$$

Here, $\mathbf{Z_{ipt}}$ is defined in Fig. 2 and derived as

$$\mathbf{Z_{ipt}} = \mathbf{V_p}/\mathbf{I_1} = \omega^2M^2/\mathbf{Z_s} + \mathbf{Z_p}. \tag{13}$$

Therefore, it has

$$\theta(\mathbf{Z_1}) = \theta(\mathbf{V_1}/\mathbf{I_1}) = \theta(\mathbf{V_p}/\mathbf{I_1}) = \theta(\mathbf{Z_{ipt}}) \tag{14}$$

Similarly,

$$\theta(\mathbf{Z_2}) = \theta(\mathbf{Z_{ipt}}). \tag{15}$$

Substituting (11)–(15) into (10), the ZVS requirement is encapsulated in the following inequality constraint:

$$\theta(\mathbf{Z_{ipt}}) > \max(\theta_1/2, \theta_2/2). \tag{16}$$

According to Table I, the variations of $\theta(\mathbf{Z_{ipt}})$ and $\max(\theta_1/2, \theta_2/2)$ are illustrated in Fig. 5 while sweeping the switching frequency. It's important to note that the frequency is normalized as $f_n = f/f_r$. When M is 22 μH, the ZVS boundary is point B [refer to (16)]. Generally, the conduction loss is minimized if $f_n = 1$. However, there are still switching losses in the bridge inverter. Increasing f introduces additional circulating energy, aiding in achieving ZVS. Eventually, a frequency of $1.8f_r$ is chosen, close to the boundary point B. When M drops, the ZVS boundary point is A. The frequency selection based on point B is still able to ensure ZVS when misalignment happens. In summary, two phases are employed to fulfill the UAV requirements and MPPT through power modulation. The frequency is carefully designed to ensure ZVS operation under dual-phase modulation.

IV. EXPERIMENT VERIFICATION

The experimental setup is shown in Fig. 6(a). The TX and RX coils are identical. The inner diameter of each coil measures 100 mm, crafted to fit the UAV landing gear. The charging area is a circle with a diameter of 200 mm. During the charging process, the vertical distance is maintained at 10 mm, as depicted in Fig. 6(b) and 6(c). The UAV would land within this designated

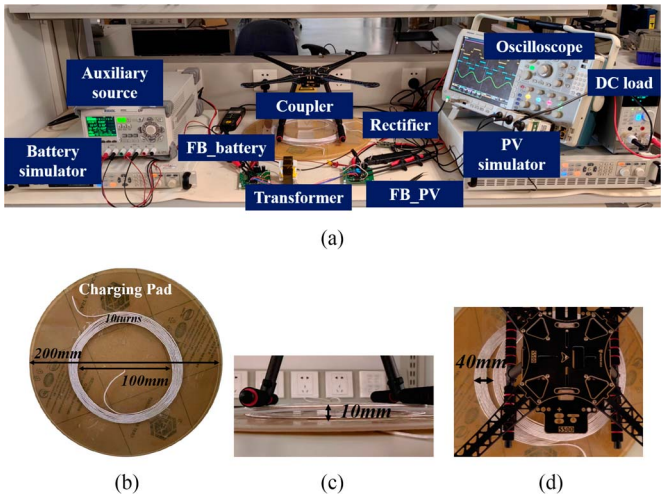

Fig. 6. Experiment platform. (a) Setup. (b) Coil. (c) Side view of coupler. (d) Top view of coupler.

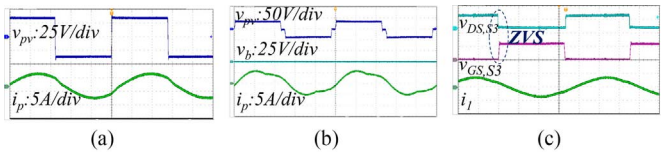

Fig. 7. Steady-state waveforms. (a) Mode 1. (b) Mode 3. (c) Switch S3.

charging area, as illustrated in Fig. 6(d), with the maximum horizontal misalignment being 40 mm.

For the target 200-W application, V_{pv}, V_b, and V_o are determined by the real demands. The voltage gain from V_{pv} to V_b directly defines the turns ratio n. For the resonant tank, only two independent parameters, L_m and L_p $(= L_s)$, need to be considered. Note that all capacitance values are calculated based on the resonance condition. L_m is selected to achieve ZVS during the dead time for both bridges. Considering the target size and misalignment conditions, the coupling coefficient remains relatively stable and could be estimated. Based on the voltage gain from V_{pv} to V_o, the necessary mutual inductance M is used to determine L_p. The system parameters are provided in Table I.

For mode 2, the maximum power is 200 W due to the collaboration of PV and battery. For a single-source scenario, such as modes 1, 3, and 4, the maximum output power is 120 W. Under mode 1, the converter operates as a LLC converter and adopts frequency modulation (FM). The terminal excitation waveform is illustrated in Fig. 7(a). Under mode 2, the terminal waveform is displayed in Fig. 8. It's noteworthy that the output currents of the two bridge inverters are identical, and only one current is shown. Under modes 3 and 4, either the PV or the battery operates. Fig. 7(b) shows the waveforms for mode 3, the curve of v_b implies battery would be shorted. The waveforms of mode 4 resembles that of Fig. 7(b) for mode 3. With eight transistors, the waveform of S_3 serves as a representative to indicate ZVS operation in Fig. 7(c). When the misalignment happens, the

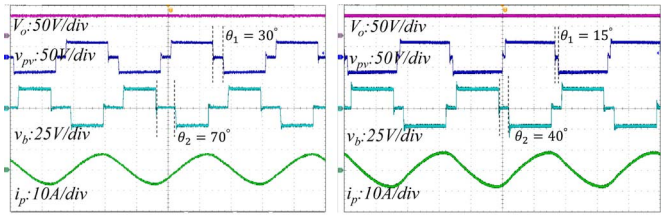

Fig. 8. Waveforms of mode 2. (a) $M = 22$ μH. (b) $M = 18$ μH.

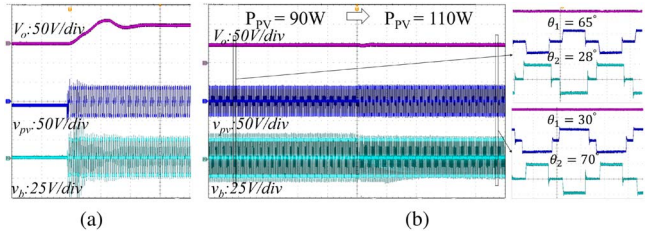

Fig. 9. Transient waveform. (a) Soft-start process of mode 2. (b) P_{pv} variation under mode 2.

phase modulation is applied to ensure MPPT and stable output as shown in Fig. 8.

The system needs to handle two types of dynamics. It transitions between modes by stopping the old mode and initiating the new mode through a soft-start process. The soft-start waveform of mode 2 is illustrated in Fig. 9(a). Within the same mode, if light conditions change, the converter undergoes another transition process. For instance, when PV power shifts from 90 to 110 W, Fig. 9(b) demonstrates how the charger redistributes the power demand of the UAV between the PV and the battery, ensuring MPPT and stable output.

The efficiency for all operational modes are depicted in Fig. 10(a). Notably, mode 1, which entails functioning as a LLC converter, exhibits the highest efficiency when employing classical frequency modulation. In mode 2, the 36-V PV independently charges the UAV. Conversely, in the absence of light, the 24-V battery charges the UAV utilizing a similar process. Due to voltage difference, the conduction losses introduced by the battery-side inverter exceed those of the PV-side inverter when delivering equivalent power. It's important to highlight that switching losses are nearly eradicated owing to ZVS, and the conduction losses of the resonant tank remain consistent due to identical P_{uav} under modes 3 and 4. Consequently, mode 4, utilizing a 24-V battery, exhibits lower efficiency compared to mode 3, utilizing a 36-V PV source. Incorporating both PV and battery in mode 2 yields an efficiency that falls between those of modes 3 and 4. Meanwhile, the black curve in Fig. 10(a) displays the phase angle θ_1 with given load range. A detailed loss breakdown of mode 2 is shown in Fig. 10(b). Misalignment leads to higher condition loss.

Table II presents a comparison of PV-battery IPT systems. In contrast to previous studies, the dual-bridge configuration proposed in this article facilitates a broader range of operational modes to address diverse scenarios. This configuration allows

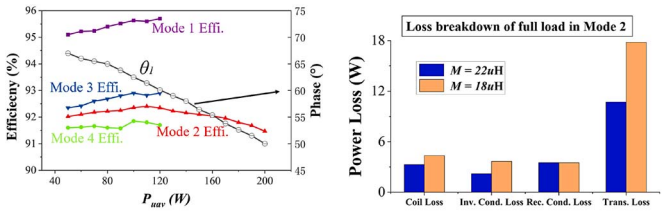

(a) (b)

Fig. 10. Loss comparison. (a) Efficiency of all modes. (b) Loss breakdown.

TABLE II
COMPARISON WITH EXISTING PV-BATTERY IPT SYSTEMS

References	[7]	[10]	[8]	[9]	This Work
Power of mode 2	20 W	378 W	120 W	200 W	200 W
Peak effi. of mode 2	85%	N/A	88.6%	89.2%	92.6%
Modulation	PWM	PWM	PSM	PWM	PSM, FM
No. of modes	2	3	3	2	4
MPPT	✓	✓	✓	✓	✓
Fully ZVS	×	×	✓	×	✓
No. of MOSFET	4	7	5	6	8
No. of inductive comp.	5	5	2	3	2
No. of capacitive comp.	8	6	6	7	4

Note: * Inductive components mean ac inductor, dc inductor, coupler, and transformer. PWM: pulse width modulation; PSM: phase shift modulation.

for the utilization of multiple modulation approaches, which collectively address various objectives such as output modulation, MPPT, and ZVS. Moreover, different operational modes share a common resonant tank, effectively reducing the number of passive components required.

V. CONCLUSION

This article introduces a three-port wireless charger designed to incorporate both PV panels and batteries for charging UAVs. By sharing the resonant tank, direct power transfer between multiple ports is facilitated, eliminating the need for redundant power stages. This setup allows for the definition of various charging modes to address real-world requirements, with multiple power flows enabling flexibility. Moreover, the phase and frequency control of the active bridges provide ample flexibility to achieve different objectives. Experimental results confirm the high-efficiency operation of the charger across multiple modes.

REFERENCES

[1] Z. Zhao, Y. Zhang, C. Li, Y. Xiao, and J. Tang, "Thermal UAV image super-resolution guided by multiple visible cues," *IEEE Trans. Geosci. Remote Sens.*, vol. 61, pp. 1–14, 2023.
[2] L. Yang, R. Zhang, Y. Bao, S. Yang, and L. Jiao, "Kernel tensor sparse coding model for precise crop classification of UAV hyperspectral image," *IEEE Geosci. Remote Sens. Lett.*, vol. 20, pp. 1–5, 2023.
[3] G. J. Lim, S. Kim, J. Cho, Y. Gong, and A. Khodaei, "Multi-UAV pre-positioning and routing for power network damage assessment," *IEEE Trans. Smart Grid*, vol. 9, no. 4, pp. 3643–3651, Jul. 2018.
[4] M. Lu, M. Bagheri, A. P. James, and T. Phung, "Wireless charging techniques for UAVs: A review, reconceptualization, and extension," *IEEE Access*, vol. 6, pp. 29865–29884, 2018.
[5] J. M. Arteaga, S. Aldhaher, G. Kkelis, C. Kwan, D. C. Yates, and P. D. Mitcheson, "Dynamic capabilities of multi-MHz inductive power transfer systems demonstrated with batteryless drones," *IEEE Trans. Power Electron.*, vol. 34, no. 6, pp. 5093–5104, Jun. 2019.
[6] I.-W. Iam, Z. Ding, Z. Huang, C.-S. Lam, R. P. Martins, and P.-I. Mak, "A flexible rooftop photovoltaic-inductive wireless power transfer system for low-voltage dc grid," *IEEE Access*, vol. 11, pp. 51117–51132, 2023.
[7] A. M. Jawad, H. M. Jawad, R. Nordin, S. K. Gharghan, N. F. Abdullah, and M. J. Abu-Alshaeer, "Wireless power transfer with magnetic resonator coupling and sleep/active strategy for a drone charging station in smart agriculture," *IEEE Access*, vol. 7, pp. 139839–139851, 2019.
[8] P. K. Chittoor and B. Chokkalingam, "Wireless electrification system for photovoltaic powered autonomous drone charging," *IEEE Trans. Transp. Electrific.*, vol. 10, no. 2, pp. 3002–3011, Jun. 2023.
[9] G. R. C. Mouli, P. V. Duijsen, F. Grazian, A. Jamodkar, and O. Isabella, "Sustainable e-bike charging station that enables ac, dc and wireless charging from solar energy," *Energies*, vol. 13, no. 14, 2020, Art. no. 3549.
[10] A. Ghosh, A. Ukil, and A. P. Hu, "PV-battery system with wireless power transfer for LV applications," in *Proc. 46th Annu. Conf. IEEE Ind. Electron. Soc. (IECON)*, 2020, pp. 4283–4287.